

Comparative study on 2,2'-bi(1,3,4-oxadiazole) derivatives: Synthesis, optical properties, SEM analysis and theoretical design

Assiya Atif^{a*}, Soukaina Ameur^{a,b}, Redouane Lakhale^c and Houssine Ait Sir^a

^aBioorganic Chemistry Team, Faculty of Sciences, Chouaib Doukkali University, El Jadida, Morocco

^bMolecular Modeling and Spectroscopy Research Team, Faculty of Sciences, Chouaib Doukkali University, El Jadida, Morocco

^cLaboratory of Physical Chemistry of Material, Department of Chemistry, Faculty of Sciences, Chouaib Doukkali University, El Jadida, Morocco

CHRONICLE

Article history:

Received July 5, 2025

Received in revised form

July 25, 2025

Accepted February 3, 2026

Available online

February 3, 2026

Keywords:

1,3,4-oxadiazole

Synthesis

Characterization

Optical Properties

Scanning Electron

Microscopy

Reactivity

ADMET

Molecular Docking

ABSTRACT

In this work, the synthesis of 6,6'-([2,2'-bi(1,3,4-oxadiazole)]-5,5'-diyl)bis(3-chloroaniline) (**6a**) and 5,5'-([2,2'-bi(1,3,4-oxadiazole)]-5,5'-diyl)bis(benzene-1,3-diamine) (**6b**) was carried out and characterized by spectral data from ¹H NMR, ¹³C NMR, IR and mass spectrometry. The optical properties of these compounds were studied, in particular the evolution of reflectance, absorption and band gap energy, and a scanning electron microscopy (SEM) analysis was performed. A comparative in-silico study combining DFT-based reactivity analysis, ADMET prediction, and molecular docking were employed for compounds 6a and 6b. Both exhibited distinct reactivity profiles and strong binding affinities toward DNA Gyrase B (7C7N) and the DNA-ruthenium complex (4E7Y), highlighting their potential as antibacterial agents, as well their potential use in photovoltaic application and for near infrared light shielding basing on the optical results.

1. Introduction

Oxadiazoles belong to the class of heterocyclic compounds and consist of one oxygen atom and two nitrogen atoms, forming a five-membered heterocyclic ring¹⁻³. 1,3,4-Oxadiazole is a furan derivative in which two carbon atoms are substituted with pyridine-type nitrogen atoms. 1,3,4-Oxadiazole derivatives exhibit a wide range of properties used in various industrial sectors. These substances possess a broad spectrum of biological activities, facilitating their use in medicine and pharmacology as active agents, including anti-inflammatory⁴, analgesic⁵, antimicrobial⁶, antiviral⁷, antifungal⁸ and antitumor⁹. A recent review focused on the antimicrobial properties of 1,3,4-oxadiazoles¹⁰. Due to their biological potential, these substances are also used in agriculture as herbicides, insecticides¹¹ and plant protection agents to control bacterial¹², viral¹³ and fungal diseases¹⁴. 1,3,4-Oxadiazole compounds also exhibit interesting optical properties¹⁵.

To explain the reactivity as well as the biological behavior of 6,6'-([2,2'-bi(1,3,4-oxadiazole)]-5,5'-diyl)bis(3-chloroaniline) (**6a**) and 5,5'-([2,2'-bi(1,3,4-oxadiazole)]-5,5'-diyl)bis(benzene-1,3-diamine) (**6b**), an in-silico analysis combine DFT Calculations, ADMET prediction and Molecular Docking, was conducted to see how the electronic characteristics correlate with the absorption, distribution, metabolism and excretion, as well as with the binding to select biological activities.

* Corresponding author

E-mail address assia.atif@gmail.com (A. Atif)

© 2026 by the authors; licensee Growing Science, Canada

doi: 10.5267/j.ccl.2026.2.001

2.2. Optical properties

Studying the light reflection and absorption behavior of materials is crucial before their use in optoelectronic devices, as their overall efficiency depends on their ability to absorb light over a range of required wavelengths.

Indeed, for both samples (**6a** and **6b**), the evolution of reflectance as a function of wavelength is almost identical (**Fig. 1**). It increases with increasing wavelength, reaching significant values in the near-infrared (NIR) range, on the order of 80 to 85%. This is very promising for the application of these two samples for near infrared light shielding.

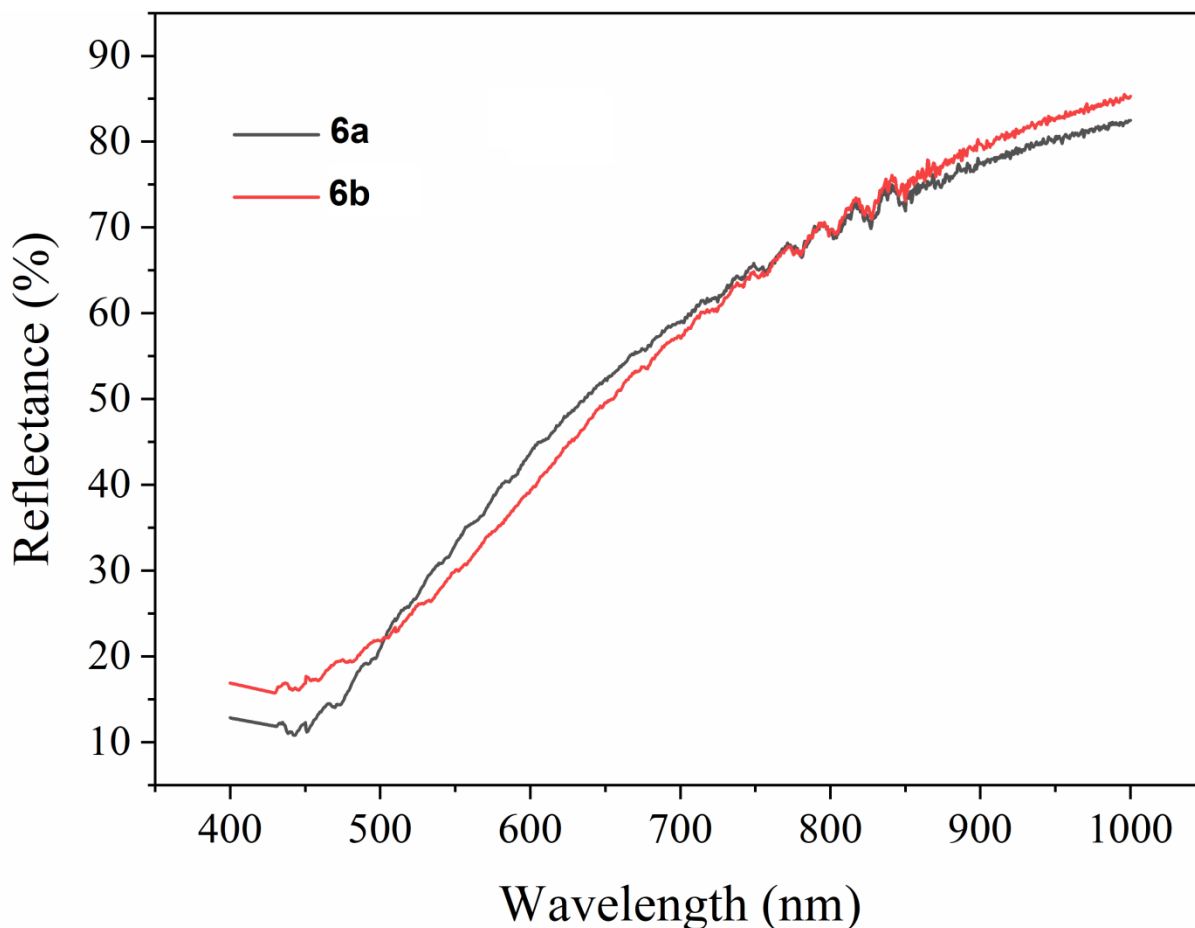


Fig. 1: Light reflection spectra in visible (Vis) and near infrared range (NIR) for (**6a**) and (**6b**)

Furthermore, according to **Fig. 2**, in the visible spectrum, specifically between 400 and 500 nm, sample (**6a**) exhibits higher absorption values than sample (**6b**). This behavior is reversed between 500 and 750 nm for both samples. However, in the near-infrared (above 750 nm), both samples show similar behavior with low absorption values. It can be concluded that the chromophores present in both samples are responsible for this absorption capacity observed in the visible spectrum. Furthermore, the optical band gap energy can be determined graphically using the following equation²⁰:

$$(\alpha \cdot h\nu)^{1/\gamma} = A (h\nu - E_g)$$

α : Absorption coefficient

h : Planck's constant

ν : photon frequency

A : constant

γ a constant related to the type of electronic transition, which is direct or indirect if γ is equal to 1/2 or 2, respectively

E_g is determined graphically by linear extraction of the region $(\alpha h\nu)^{1/n}$ depending on $(h\nu)$ on the X axis.

After adjustment, we found that the optical band gap energy of both samples is direct. According to **Figure 3**, the direct band gap energy values correspond to 2.23 to 2 eV for (**6a**) to (**6b**), respectively. This suggests a promising application of these samples, in particularly (**6b**) in the photovoltaic field, which requires low band gap energy values.

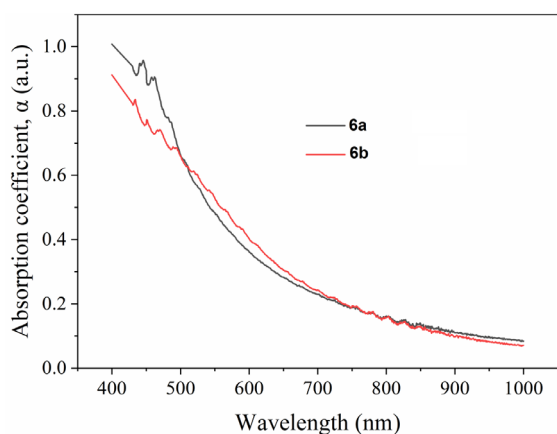


Fig. 2. Absorption spectra in visible and near infrared range for **(6a)** and **(6b)**

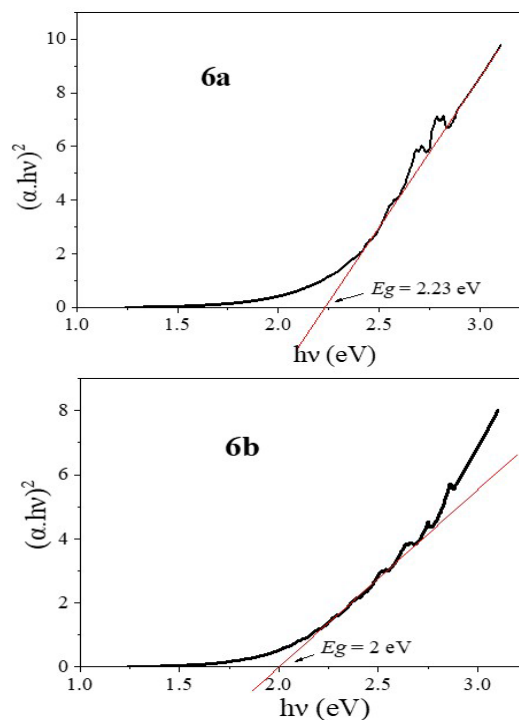


Fig. 3. Tauc plots for **(6a)** and **(6b)**

2.3. Scanning electron microscopy (SEM)

The morphology of samples **(6a)** and **(6b)** was analyzed by scanning electron microscopy (SEM) at different magnifications (**Fig. 4**). These results clearly indicate that sample **(6a)** has a rougher surface than **(6b)**. The latter appears more crystalline than **(6a)** because it shows particles in the form of fine flakes after magnifications of 100 μ m (**1**) and 10 μ m (**2**).

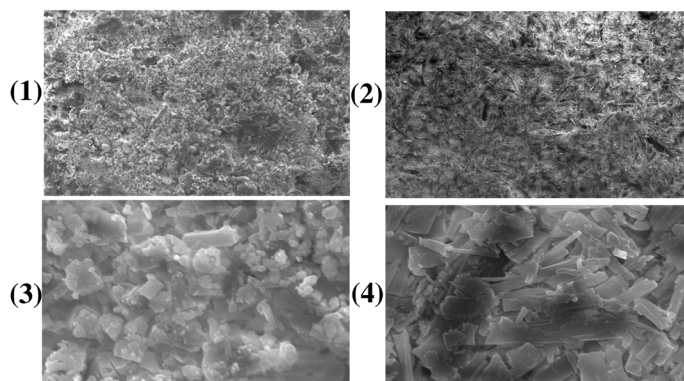


Fig. 4. SEM images at 100 μ m (**1**, **2**) and 10 μ m (**3**, **4**) for **6a** (**1**, **3**) and **6b** (**2**, **4**)

2.4. Theoretical Analysis of Chemical Reactivity of **6a** and **6b**

The HOMO/LUMO analysis and corresponding global reactivity indices of compounds **6a** and **6b** indicate that they exhibit different properties regarding their susceptibilities toward undergoing chemical reactions.

Table 1. Chemical hardness η , chemical electron potential μ , electrophilicity ω , nucleophilicity index N , HOMO and LUMO energies, Gap energy (ΔE) of the two compounds **6a** and **6b**.

	LUMO (u.a)	HOMO (u.a)	(ΔE)	Ω (eV)	η (eV)	N (eV)	μ (eV)
6a	-0.09308	-0.23239	3.79	5.17	1.89	3.40	-4.425
6b	-0.07624	-0.21074	3.66	4.15	1.83	3.99	-3.90

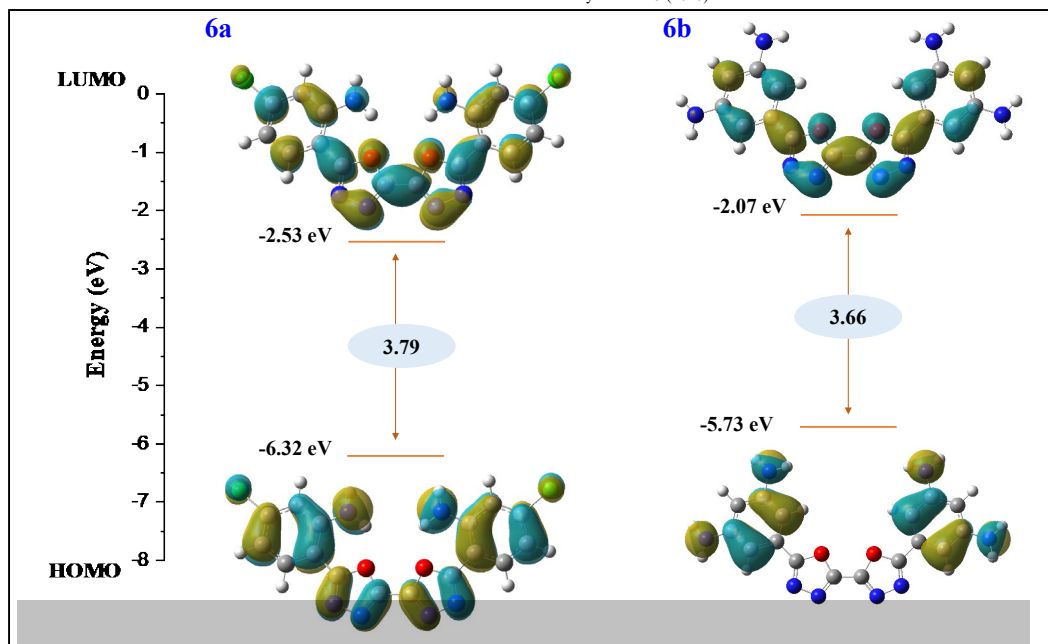


Fig. 5. Comparison of HOMO, LUMO, and Energy Gap (ΔE) for Compounds **6a** and **6b**

From the analysis of frontier molecular orbital energy levels, we found that compound **6b** had a higher HOMO value (-5.73 eV) compared to that of compound **6a** (-6.32 eV), which shows that compound **6b** has a stronger ability to donate electrons and is therefore more nucleophilic than compound **6a**. On the other hand, compound **6a** had a lower LUMO energy (-2.53 eV) than that of compound **6b** (-2.07 eV), indicating that compound **6a** is more likely to accept electrons and has greater electrophilicity than compound **6b**. The energy gap for **6b** was slightly smaller (3.66 eV) than for compound **6a** (3.79 eV), indicating that **6b** may be marginally more reactive than compound **6a**, but its greater hardness ($\eta = 1.89$ eV vs 1.83 eV) suggests that compound **6a** is more stable than compound **6b**. However, the chemical potential and global electrophilicity index confirmed that compound **6a** was much more electrophilic ($\mu = -4.43$ eV, $\omega = 5.17$ eV) than was compound **6b** ($\mu = -3.99$ eV, $\omega = 3.40$ eV).

The compound **6a** acts primarily as a stable electrophile, while compound **6b** functions primarily as a nucleophile and is thus slightly more reactive in the presence of electrophilic species.

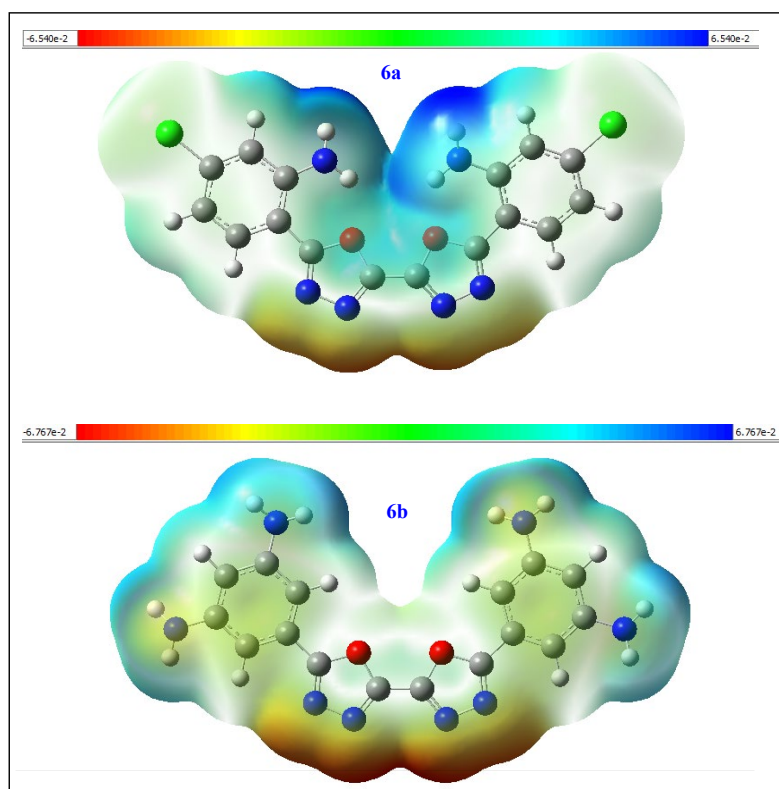


Fig. 6. Molecular Electrostatic Potential (MEP) Surface Visualization of Compounds **6a** and **6b**

Molecular Electrostatic Potential (MEP) of Compounds **6a** and **6b** (Fig 6) show that there is a very clear electrical polarization of the electron density throughout these compounds' molecular structures. The carbonyl oxygen atom and the heteroatoms (N and O) are where the most negative electrostatic potential occurs, which are likely to be the preferred electrophilic attack sites and the most favourable hydrogen bond acceptor sites for both compounds. The blue areas of the MEP correspond to areas of the molecule that have little or no electron density, which in this case are due to hydrogen atoms and fragments that are less electronegative. These regions will be able to interact through weak donor or electrostatic interactions with other compounds. Compared to Compound **6a**, Compound **6b** has a greater extent of the negative potential and therefore has a greater amount of electron density and polarity that may assist it to participate in electrostatic and hydrogen bond interactions with biological targets. In general, the distribution of MEP suggests that the heteroatom-rich regions dominate the reactivity and intermolecular interaction behaviour of both compounds, providing a strong basis for the predicted docking affinities and biological activities of these compounds.

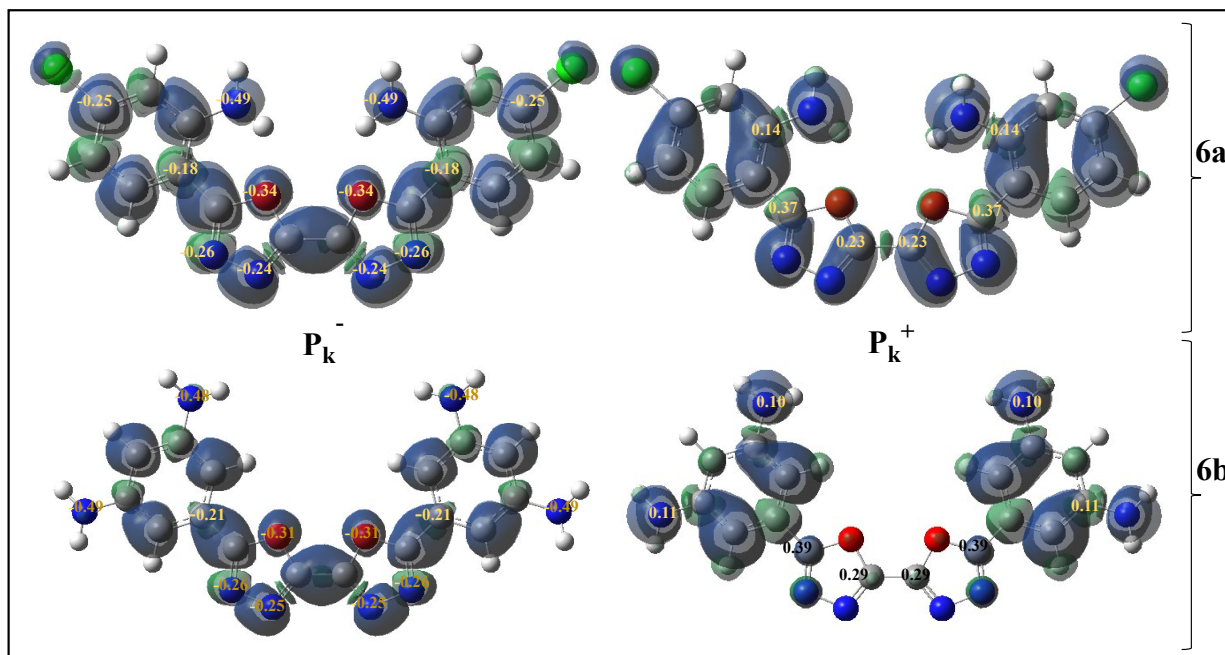


Fig. 7. Spin density maps of Parr functions illustrating the pK^+ and pK^- reactive sites for compounds **6a** and **6b**

Compound **6a**'s pK^- assessment, as detailed below, determined that N13 and N33 are the primary nucleophilic sites, whereas carbonyl oxygen atoms (O5 and O22) act as secondary sources for nucleophiles. Other nitrogen and conjugated carbon atoms show variations of nucleophilic behavior and impact regional selectivity or intermolecular interactions.

C1 and C23 (as identified through the pK^+ evaluation) are the most electrophilic parts of this compound; these positions are therefore where nucleophiles will preferentially react. Conversely, C4 and C6 are the next preferred reactions among the carbon sources. A number of H atoms possess significant pK^+ values, indicating their potential involvement in hydrogen-bond donation and intermolecular stabilization.

As for **6b**, the N-enriched terminal region (N29–N32) has the highest pK^- values of all of the components, representing the greatest source for nucleophile capacity; oxygen acts next, albeit at lower tendencies.

Analysis via pK^+ clearly indicates that C1 and C17 are the zones of highest electrophilicity for this compound; these areas provide the highest likelihood for nucleophilic intervention in the compound. Other carbon positions (C4 and C6) indicate lower levels of electrophilicity but, similar to **6a**, are all carbon sources and are therefore primarily carbon-based nucleophiles. Similarly, numerous H atoms are in very active configurations (H-atoms) that act in support of H-bond formation and intermolecular stabilization with regard to nitrogens in both compounds.

The populations of ELF (Fig 8) indicate where the most significant electron donating and bond polarizing sites of **6a** and **6b** are located, as well as where electron flow occurs and how electron density distributes throughout the entire molecule.

The ELF analysis of compounds **6a** and **6b** reveals that the oxygen atoms (O1 and O2) are the sites of highest electron density, with their populations being approximately 4.2 to 4.3 electrons. Therefore, it is concluded that oxygen is a significant nucleophile for these compounds. In addition to oxygen, nitrogen (N1, N2, N5, and N8) was determined from the analysis to have a substantial amount of electron density (1.6–3.1 electrons). Thus, nitrogen was classified as a nucleophile, although only a secondary nucleophile compared to oxygen. Additionally, the covalent C–H bonds of **6a** and **6b** have a population near two electrons, indicating that these bonds are adequately localized; however, the populations of electrons in the intermediate C–C and C–N bonds (2.4–3.1 electrons) exhibit partial delocalization, particularly within the

conjugated portions of the compounds, which results in increased stability for both molecules. The polar bonds of **6a** and **6b** (C–O and C–Cl), as expected, show greater electron density near the more electronegative atoms of carbon and chlorine, indicating both the polar nature of these bonds and their potential for reactivity.

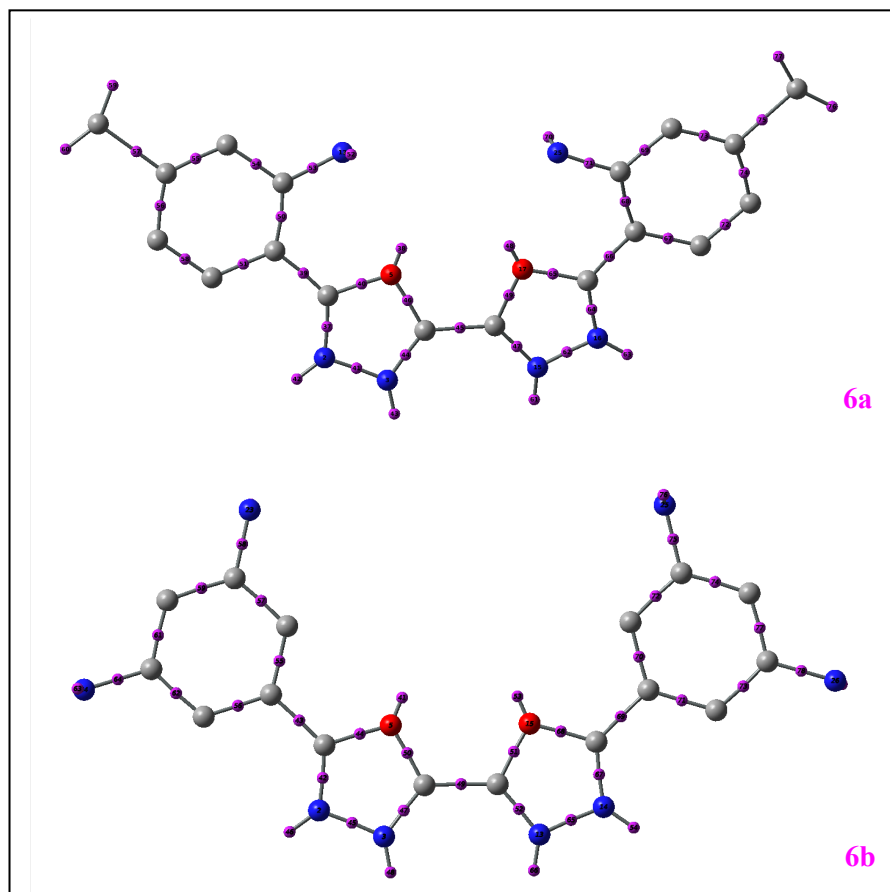


Fig. 8. Electron Localization Function (ELF) visualizations illustrating the distribution and localization of electrons in compounds **6a** and **6b**

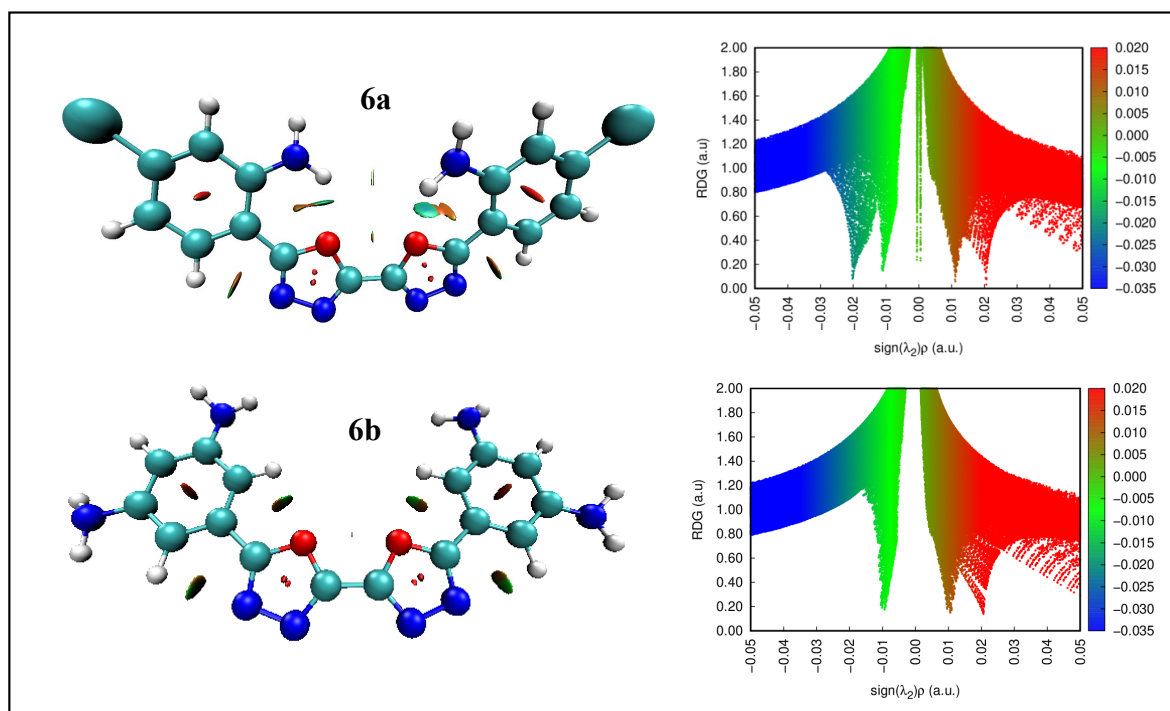


Fig. 9. RDG/NCI Analysis of Compounds **6a** and **6b** Highlighting Non-Covalent Interactions

The RDG (Reduced Density Gradient) and NCI (Non-Covalent Interaction) analysis provides insight into the nature and strength of non-covalent interactions in compounds **6a** and **6b**. The colour map has assigned a blue colour to areas of strong attractive interaction (hydrogen bonds), green areas representing weak van der Waals type interactions (dispersion forces, π - π stacking, etc.) and red areas representing repulsive steric interactions. For compound **6a**, it can be seen that most of the RDG colour map consists of green colour indicating an abundance of van der Waals contact between molecular fragments stabilizing the dimer or conformation of the fragment; additionally, there are some small areas of blue which may indicate the presence of hydrogen bonds between the nitrogen and oxygen of the molecule, and there are a few limited areas of red which indicate little steric repulsion. With compound **6b**, the RDG colour map has similar patterns to that of compound **6a**: with the green regions indicating van der Waals interaction, but somewhat more localized than that observed for compound **6a**. Additionally, blue regions are indicative of possible hydrogen bonding, with significantly less pronounced blue areas indicating weaker or fewer directional interactions. These observations collected from the RDG and NCI analysis has assisted in planning future molecular docking experiments to help identify potential binding sites and interaction hotspots for target proteins.

2.5. ADMET Properties and Docking-Redocking Validation of Compounds **6a** and **6b**

Examining ADME parameters (Table 2) indicates pharmaceutical differences in two compounds (**6a** and **6b**). Compound **6a** has the highest lipophilicity with XLOGP3 of 3.01 and moderate polar surface area; therefore, predicted to have highest gastrointestinal absorption due to one Lipinski rule violation due to molecular weight. Compound **6b** has much higher overall polarity, as shown by its high TPSA and ability to form many hydrogen bonds, and therefore, predicted to have minimal gastrointestinal absorption. Both compounds are predicted not to be permeant to the blood-brain barrier and likely P-gp substrates, indicating limited exposure to the central nervous system and possible efflux. In addition, both compounds have been found to have aniline structural alerts. Therefore, compound **6a** is predicted to have better oral absorption properties than compound **6b**; however, compound **6b** is anticipated to be more soluble in aqueous solutions and have stronger intermolecular interactions compared to compound **6a**, which could affect how each compound binds in molecular docking.

Table 2. Comparative ADME parameters of compounds **6a** and **6b**

Parameter	6a	6b
Molecular weight (MW)	> 350 g·mol ⁻¹	350.33 g·mol ⁻¹
Log P (XLOGP3)	3.01	-0.12
TPSA (Å ²)	Moderate (< 100 Å ²)	181.92 Å ²
H-bond donors (HBD)	2	4
H-bond acceptors (HBA)	5	6
Lipinski's rule violations	1 (MW > 350)	0
GI absorption	High	Low
BBB permeant	No	No
P-gp substrate	Yes	Yes

Compounds **6a** and **6b** have predicted toxicity profiles that share and differ in some ways (Table 3). Compound **6b** has been predicted as AMES toxic; however, Compound **6a** is not flagged as a mutagenic. Their predicted activities against hERG I suggest they are both noninhibitors of hERG I; however, their activities against hERG II suggest they both have the potential to inhibit hERG II giving them both equal risk of cardiac liability. The values for acute oral toxicity (LD₅₀) for both Compounds are quite comparable indicating that they both possess a similar risk of short-term toxicity; however, Compound **6b** is also predicted to have a higher TMAX [maximum tolerated dose] in humans than Compound **6a** and a higher chronic toxicity threshold (LOAEL) than Compound **6a**; this suggests a greater degree of safety with prolonged exposure. Both Compounds have predicted hepatotoxicity, but neither are predicted to produce skin sensitization. When environmental predictions are considered, the predictions of Tetrahymena pyriformis toxicity from both Compounds are identical, but the predicted toxicity towards fish differs greatly, with Compound **6a** predicted to have a greater toxicity to minnows than Compound **6b**.

Table 3. Comparative toxicity profile of compounds **6a** and **6b**

Toxicity parameter	6a	6b
AMES toxicity	No	Yes
Max. tolerated dose (human)	0.244 log mg/kg/day	0.951 log mg/kg/day
hERG I inhibitor	No	No
hERG II inhibitor	Yes	Yes
Oral Rat Acute Toxicity (LD ₅₀)	2.726 mol/kg	2.788 mol/kg
Oral Rat Chronic Toxicity (LOAEL)	0.779 log mg/kg_bw/day	2.285 log mg/kg_bw/day
Hepatotoxicity	Yes	Yes
Skin sensitisation	No	No
T. pyriformis toxicity	0.285 log µg/L	0.285 log µg/L
Minnow toxicity	-1.192 log mM	2.057 log mM

The toxic potential of both Compounds resulted in the execution of molecular docking studies to assess the binding affinity and interaction profile of the two Compounds against two of the selected bacterial targets; DNA Gyrase B (7C7N) and the DNA-ruthenium complex (4E7Y). The use of toxicity predictions is a common practice in the early stages of drug discovery; however, it does not remove the need to investigate the target-ligand interactions. The objective of the docking work is to gain insight into the mechanism of antibacterial activity demonstrated by the bis-1,3,4-oxadiazole derivatives, while the consideration of toxicity serves to highlight possible areas for improvement in compound structure rather than being disqualified from being explored at this stage.

Molecular docking targets DNA Gyrase B (PDB ID: 7C7N) and the DNA-ruthenium complex (PDB ID: 4E7Y) were chosen based on the molecular structure and physicochemical properties of bis-1,3,4-oxadiazole derivatives assessed in this study. The chemical structure of the compounds 6a and 6b demonstrates rigid structures with planar aromatic components and multiple heteroatoms (N, O) capable of forming multiple hydrogen-bonding interactions and establishing favorable electrostatic interactions in the well-defined pockets of the target structures. It has been established that DNA Gyrase B is an effective antibacterial target for which the identified binding site also represents a sufficient binding site for heterocyclic and aromatic inhibitors, both polar and hydrophobic in nature, which would augur the oxadiazole scaffold. The availability of high-resolution co-crystallized 4E7Y structures presented an opportunity to further investigate the mode of action of the fatty acid-derivative plan oxadiazole molecules by taking advantage of the DNA binding site of structurally defined DNA-ruthenium complexes, enabling further analysis of intercalation and electrostatic interactions associated with antibacterial activity. The identification of high-resolution co-crystallized structures validates both PDB IDs 7C7N and 4E7Y as appropriate models for the evaluation of antibacterial effects and various structural formats.

It is a necessary validation step to redock the co-crystallized ligand before docking new compounds. The reliability of docking protocol was evaluated using the experimentally known confirmation as a reference. Redockings of DNA Gyrase B (7C7N), and the DNA-Ru complex, 4E7Y) resulted in RMSDs of 0.43 Å, and 0.23 Å, respectively for comparison with the native structures (Fig 10). These small RMSD values demonstrate that the docking protocol is able to truly reproduce the experimentally known binding modes, and this instills confidence for the further docking of 6a and 6b.

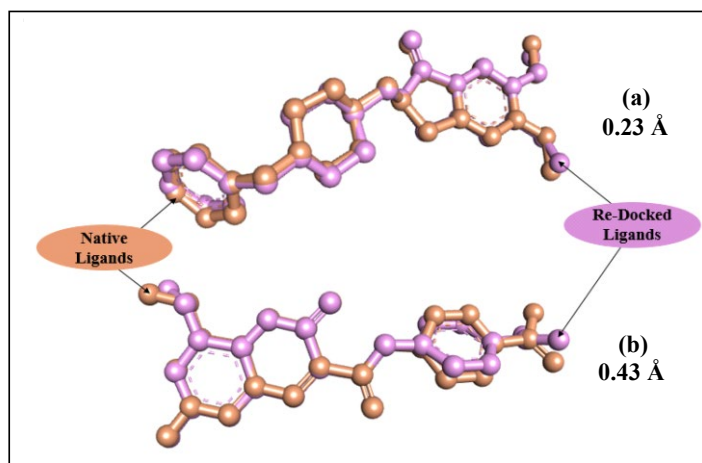


Fig. 10. Validation of Docking Protocol: Superposition of Native and Redocked Co-Crystallized Ligands in 7C7N (b) and 4E7Y (a)

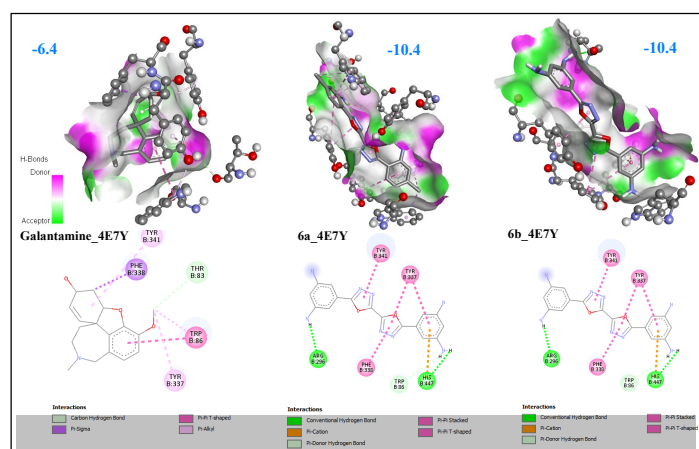


Fig. 11. 2D Interaction and Hydrogen Bond Analysis of Galantamine and Compounds 6a/6b Docked into Acetylcholinesterase (4E7Y): Comparative Binding Affinities (kcal/mol)

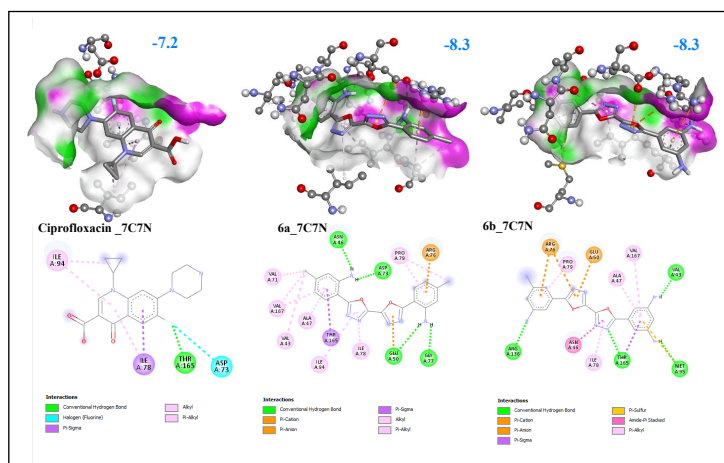


Fig. 12. 2D Interaction and Hydrogen Bond Analysis of Ciprofloxacin and Compounds 6a/6b Docked into DNA Gyrase (7C7N): Comparative **Binding Affinities (kcal/mol)**

The molecular docking studies show that **6a** and **6b** bind effectively to both target proteins, DNA Gyrase B (7C7N) and the DNA-Ru complex (4E7Y). For DNA Gyrase B (7C7N), **6a** and **6b** have an identical binding affinity of -8.3 kcal/mol, which is higher than that of the reference ligand, Ciprofloxacin (-7.2 kcal/mol) and shows the potential for increased antibacterial activity. For the DNA-Ru complex (4E7Y), both **6a** and **6b** have a binding affinity that is much greater than that for Galantamine (-6.4 kcal/mol). -10.4 kcal/mol indicates strong neuroprotective interactions. The data support the conclusion that both compounds 6a and 6b bind to the target proteins effectively, better than the reference ligands, providing support for their predicted biological activity.

3. Conclusion

This study confirms the structure of 6,6'-([2,2'-bi(1,3,4-oxadiazole)]-5,5'-diyl)bis(3-chloroaniline) (**6a**) and 5,5'-([2,2'-bi(1,3,4-oxadiazole)]-5,5'-diyl)bis(benzene-1,3-diamine) (**6b**) by ^1H NMR, ^{13}C NMR, mass spectrometry and FTIR-ATR infrared spectroscopy. The reflectance of these compounds (**6a** and **6b**) increases with increasing wavelength, reaching significant values in the near-infrared (NIR) range of 80 to 85%. This shows the possible application of the synthesized organic samples for NIR light shielding. Also, both the samples, in particular (**6b**) demonstrate a promising application in photovoltaics. Scanning electron microscopy (SEM) analysis clearly indicates well crystallized particles of sample (**6b**), in contrast to sample (**6a**) which showed rougher surface. The results of both, DFT Calculations for reactivity with Molecular Docking analyses, suggest that **6a** is both less reactive (Electrophilic) and more stable than **6b** (Nucleophilic) and provides unique chemical interaction patterns for both oxadiazole derivatives. The results show that both oxadiazole derivatives have significant binding potential, suggesting further evaluation of their use for potential biomedical applications.

4. Experimental

4.1. Materials and Methods

All reagents and solvents were obtained from Sigma Aldrich and used as received. Reaction progress is monitored by thin-layer chromatography (TLC) on aluminum sheets coated with Merck 60 F254 silica gel (thickness 0.2 nm). Revelation is carried out under a UV-Visible lamp (at 254 and 365 nm). The melting points of the synthesized compounds were determined using a Köfler bench to degrees Celsius. FTIR spectra were recorded on a SHIMADZU FT-IR 8400S spectrometer with a Smart iTR accessory and attenuated with total reflection crystal diamond (ATR) in the range (500-4000 cm^{-1}). Spectra were recorded on a Fourier transform JNM-ECZ500/S1 FT NMR SYSTEM (JEOL) (500 MHz for proton and 125 MHz for carbon 13) at the Centre National pour la Recherche Scientifique et Technique (CNRST) in Rabat. High-resolution mass spectrometry (HRMS) was performed using an Ultimate 3000-Exactive Plus Thermo quadrupole-Orbitrap mass spectrometer, equipped with a collision cell, also housed at the CNRST in Rabat.

4.2. Operating conditions of optical properties

A Shimadzu UV-160 A spectrophotometer was used for optical measurements.

4.3. Operating conditions of scanning electronic microscopy (SEM)

Scanning electron microscopy (SEM) was performed using a Hirox SH-5500P microscope, equipped with a GEMINI field emission gun (FEG), operating at an accelerating voltage of 15 kV and a working distance of 5 mm.

4.4. General Procedure

4.4.1. Synthesis of dimethyl oxalate (3)

To synthesize dimethyl oxalate (**3**), 7 mmol of oxalic acid (**1**) were dissolved in 30 mL of methanol (**2**), and then 8 mL of thionyl chloride were added at 0 °C. The reaction mixture was refluxed for six hours. After the reaction was complete, the mixture was neutralized to pH 7 using a 10% NaHCO₃ solution until a pH of 7 was reached. This was followed by liquid-liquid extraction with ethyl acetate. Dimethyl oxalate (**3**) was obtained in liquid form by evaporation of this compound¹⁶. *Colorless Liquid, 91%, ¹H NMR(500MHz/DMSO-d₆,ppm): 3.62(s,6H,CH₃), ¹³C NMR (125MHz/DMSO-d₆, ppm) : 156.66(2C=O), 56.56(2CH₃), IR (cm⁻¹): 1712 νC=O, 1267 νC-H, 1102 νC-O, MS(ESI): m/z = 119 [M+H]⁺, Found, %: C 40.67; H 5.07. C₄H₆O₄. Calculated, %: C 40.68; H 5.08.*

4.4.2. Synthesis of oxalohydrazide (4)

Seven mmol of dimethyl oxalate (**3**) was treated with 10 mL of hydrazine hydrate by stirring at room temperature for 18 hours. The reaction mixture was then concentrated and subjected to several triturations with methanol to remove excess hydrazine hydrate. The solid was finally recrystallized from ethanol, yielding a white powder¹⁷. *Solid White, 86%, m.p: 242°C ¹H NMR(500MHz/DMSO-d₆,ppm): 4.81(s,4H,NH₂), 9.32(s,2H,NH), ¹³C NMR (125MHz/DMSO-d₆, ppm) : 157.00(2C=O), IR (cm⁻¹): 3204 νN-H, 3061-3111 νNH₂, 1721 νC=O, MS(ESI): m/z = 119 [M+H]⁺, Found, %: C 20.35; H 5.07; N 47.47. C₂H₆N₄O₂. Calculated, %: C 20.34; H 5.08; N 47.46.*

4.4.3. Synthesis of 6,6'-([2,2'-bi(1,3,4-oxadiazole)]-5,5'-diyl)bis(3-chloroaniline) (6a) and 5,5'-([2,2'-bi(1,3,4-oxadiazole)]-5,5'-diyl)bis(benzene-1,3-diamine) (6b)

Three millimoles of oxalohydrazide (**4**) are added to a solution of 6 millimoles of an acid derivative (**5**) in 15 mL of phosphoryl trichloride. The mixture is boiled under reflux for six hours. After cooling, the mixture is neutralized with a 25% ammonia solution until a pH of 7 is reached. The precipitate formed is filtered and recrystallized in ethanol¹⁸.

6a: 6,6'-([2,2'-bi(1,3,4-oxadiazole)]-5,5'-diyl)bis(3-chloroaniline)

Solid beige, 96%, m.p >300°C, ¹H NMR(500MHz/DMSO-d₆,ppm): 5.74(s,4H,NH₂), 7.38(d,2H,CHar), 7.60(d,2H, CHar), 7.78(s,2H, CHar). ¹³C NMR (125MHz/DMSO-d₆, ppm): 164.46(2C=N), 163.59(2C=N), 147.30(2Car), 132.89(2Car), 128.28(2Car), 121.64(2Car), 117.55(2Car), 116.74(2Car). IR (cm⁻¹): 3125-3202 νNH₂, 1664 νC=N, MS(ESI): m/z = 389 [M+H]⁺, Found, %: C 49.47; H 2.59; N 21.64. C₁₆H₁₀N₆O₂Cl₂. Calculated, %: C 49.48; H 2.58; N 21.65.

6b: 5,5'-([2,2'-bi(1,3,4-oxadiazole)]-5,5'-diyl)bis(benzene-1,3-diamine)

Solid brown, 87%, m.p >300°C, ¹H NMR(500MHz/DMSO-d₆,ppm): 5.40(s,8H,NH₂), 7.26(s,2H,CHar), 7.46(s,4H, CHar). ¹³C NMR (125MHz/DMSO-d₆, ppm): 161.46(2C=N), 161.04(2C=N), 148.35(4Car), 127.30(2Car), 111.71(4Car), 104.51(2Car). IR (cm⁻¹): 3032-3117 νNH₂, 1625 νC=N, MS(ESI): m/z = 351 [M+H]⁺, Found, %: C 54.85; H 4.01; N 32.01. C₁₆H₁₄N₈O₂. Calculated, %: C 54.86; H 4; N 32.

4.5. Theoretical and Computational Methods

This study used Density Functional Theory (DFT) because of its balance between the computational accuracy and computer efficiency²¹⁻²³. DFT is one of the techniques used most often to study chemical and electronic reaction mechanisms and has produced a substantial increase in the number of theoretical studies based on its use. Gaussian 09²⁴ was used to perform the DFT calculations²⁵, with the graphical interface GaussView 6.0.16. The B3LYP/6-311G(d,p)²⁶ method was utilized to optimize all stationary point geometries, as this method has demonstrated reliable performance in accurately describing frontier molecular orbital energies and global reactivity descriptors of heterocyclic systems²⁶. The starting materials, **6a** and **6b**, were initially optimized using gas phase calculations. The HOMO and LUMO energies were determined from the optimized structures of the compounds; then the energy gap was calculated as $\Delta E = E(\text{LUMO}) - E(\text{HOMO})$. The global electrophilicity (ω) and nucleophilicity (N) indices were determined following established conceptual DFT approaches^{27,28}. The electrophilicity was computed using the relation $\omega = (\mu^2/2\eta)$, whereas the nucleophilicity index was evaluated relative to tetracyanoethylene (TCE) as a reference²⁹ electrophile according to $N = E_{\text{HOMO}}(\text{molecule}) - E_{\text{HOMO}}(\text{TCE})$. The electronic chemical potential (μ) and chemical hardness (η) were taken from the energies of the frontier molecular orbitals (HOMO and LUMO) using the standard expressions $\mu = (E_{\text{HOMO}} + E_{\text{LUMO}})/2$ and $\eta = (E_{\text{LUMO}} - E_{\text{HOMO}})/2$. The molecular electrostatic potential (MEP) surface²⁷ was generated on the electron density isosurface using the optimized geometry obtained after complete geometry optimization. Parr reactivity functions, which are widely employed to identify nucleophilic and electrophilic sites in heterocyclic systems and have been successfully applied to bis-(5-membered heterocyclic) compounds^{30,31}, were used in this study to estimate the electrophilic and nucleophilic reactivity of both compounds, allowing the identification of the most reactive sites in each molecule³². Subsequently, the Electron Localization Function (ELF) analyses³³ were performed using TopMod and Multiwfn, and SMILES representations of both compounds were developed in order to predict the ADME properties of each compound with the SwissADME program.³⁴

The compound toxicity profiles were predicted with pkCSM³⁵. Molecular docking studies were conducted following a validated redocking protocol of the co-crystallized ligand³⁶ allowing validation of the docking grid parameters and confirmation of proper active-site recognition.

Acknowledgements

The authors are grateful to for the research assistance from Bioorganic Chemistry Team, Molecular Modeling and Spectroscopy Research Team and Laboratory of Physical Chemistry of Material, Faculty of Sciences, Chouaib Doukkali University, El Jadida, Morocco.

Declaration of competing interest: The authors declare no conflicts.

Finding: No external funding was received for this research paper.

Data availability statement: No data was used for the research described in the article.

References

- Kacka-Zych A. (2025) Synthesis of heterocycles via cycloaddition reactions with the participation of cyano-substituted nitroalkenes. *Chem. Heterocycl. Compd.*, 61(7/8) 317-319.
- Jasiński R. (2025) Recent progress in the synthesis of nitropyrazoles and their hydrogenated analogs via noncatalyzed (3+2) cycloaddition reactions of conjugated nitroalkenes. *Chem. Heterocycl. Compd.*, 61(7/8) 286-289
- Janowski M., Demchuk O. M., and Wujec M. (2025) Antibacterial efficiency of compounds bearing 1, 2, 3-triazole scaffold: a critical review. *Chem. Heterocycl. Compd.*, 61(7/8) 290-302
- Szandruk-Bender M., Merwid-Ląd A., Wiatrak B., Danielewski M., Dzimira S., Szkudlarek D., Szczukowski L., Swiatek P., and Szelağ A. (2021) Novel 1, 3, 4-oxadiazole derivatives of pyrrolo [3, 4-d] pyridazinone exert anti-inflammatory activity without acute gastrotoxicity in the carrageenan-induced rat paw edema test. *J. Inflamm. Res.*, 21(24) 5739-5756.
- Abd-Ellah H. S., Abdel-Aziz M., Shoman M. E., Beshr E. A., Kaoud T. S., and Ahmed A. S. F. (2016) Novel 1, 3, 4-oxadiazole/oxime hybrids: Synthesis, docking studies and investigation of anti-inflammatory, ulcerogenic liability and analgesic activities. *Bioorg. Chem.*, 69(16) 48-63.
- Patel N. B., and Patel J. C. (2010) Synthesis and Antimicrobial Activity of 3-(1, 3, 4-Oxadiazol-2-yl) quinazolin-4 (3H)-ones. *Sci. Pharm.*, 78(2) 171-193.
- Li Z., Zhan P., and Liu X. (2011) 1,3,4-Oxadiazole: A privileged structure in antiviral agents. *Mini-Rev. Med. Chem.*, 11(13) 1130-1142.
- Zhang M. Z., Mulholland N., Beattie D., Irwin D., Gu Y. C., Chen Q., Yang G., and Clough J. (2013) Synthesis and antifungal activity of 3-(1, 3, 4-oxadiazol-5-yl)-indoles and 3-(1, 3, 4-oxadiazol-5-yl) methyl-indoles. *Eur. J. Med. Chem.*, 63(13) 22-32.
- Savariz F. C., Foglio M. A., Ruiz A. L. T. G., da Costa W. F., de Magalhães Silva M., Santos J. C. C., Figueiredo I. M., Meyer E., Carvalho J. E., and Sarragiotto M. H. (2014) Synthesis and antitumor activity of novel 1-substituted phenyl 3-(2-oxo-1, 3, 4-oxadiazol-5-yl) β -carboline and their Mannich bases. *Bioorg. Med. Chem.*, 22(24) 6867-6875.
- Chaudhary T., Upadhyay P. K., and Kataria R. (2024) Anti-inflammatory and Antimicrobial Potential of 1, 3, 4-oxadiazoles and its Derivatives: A Review. *Curr. Org. Synth.*, 21(8) 1014-1020.
- Turaeva S. M., Ismailova D. S., Khasanov S. S., Nurmakhmadova P. A., Elmuradov B. Z., Azimova S. S., and Juraev D. T. (2024) Studies on insecticidal activities of 2-benzylthio-5-(4-Aminophenyl)-1, 3, 4-oxadiazole against *Helicoverpa armigera*. *Bulg. J. Agric. Sci.*, 30(6) 1059-1066.
- Prabhakar G., and Domala R. (2024) Design, Synthesis, Characterization, Docking and Biological Assessment of Innovative 5-(Pyrazin-2-yl)-1, 3, 4-oxadiazol-2-amine Derivatives for Enhanced Anti-fungal and Anti-Bacterial Activities. *Res. J. Pharm. Technol.*, 17(10) 5023-5030.
- Shin Y., Park C. M., Kim D. E., Kim S., Lee S. Y., Lee J. Y., Jeon W. H., Kim H. G., Bae S., and Yoon C. H. (2024) Discovery of new acetamide derivatives of 5-indole-1, 3, 4-oxadiazol-2-thiol as inhibitors of HIV-1 Tat-mediated viral transcription. *Antimicrob. Agents. Chemother.*, 68(10) e00643-24.
- Yao L., Zhang G., Yu L., Liu S., Wang X., Fan T., Kang H., and Feng W. (2022) Development of 1, 3, 4-Oxadiazole derived antifungal agents and their application in maize diseases control. *Front. Plant Sci.*, 13(22) 912091-912101.
- ŞAŞ E. B. (2025) Optical, non-linear optical and electronic properties of 1, 3, 4-oxadiazole derivative: a combined experimental and theoretical study. *J. Mater. Sci.: Mater. Electron.*, 36(20) 1241-1255.
- Shekarchi M., Navidpour L., Khorami A. R., Partoazar A., Shafaroodi H., Rahmanipour N., Shafiee A., and Shekarchi M. (2011) Synthesis of N-arylidene-2-(2-phenoxyphenyl) acetohydrazides as anti-inflammatory agents. *Iran. J. Pharm. Res.*, 10(2) 369-377.
- Galal S. A., Hegab K. H., Kassab A. S., Rodriguez M. L., Kerwin S. M., El-Khamry A. M. M. A., and El Diwani, H. I. (2009) New transition metal ion complexes with benzimidazole-5-carboxylic acid hydrazides with antitumor activity. *Eur. J. Med. Chem.*, 44(4) 1500-1508.

18. Atif A., Marghich M., Nabil N., El Alami A., Daoudi N., Harit T., Youssoufi F., Salah M., Bitar A., and Ait Sir H. (2025) Design, synthesis, and antidiabetic evaluation of novel 1,3-di(1,3,4-oxadiazol-2-yl)benzene derivatives as potent pancreatic α -amylase inhibitors: In vitro and in silico approaches. *Curr. Chem. Lett.*, 15(1) 175-192
19. Atif A., El Alami A., Youssoufi F., Jebbari S., and Ait Sir H. (2025). Review of synthesis process of 1,3,4-oxadiazole analogs. *Curr. Chem. Lett.*, 14(2) 339–364
20. Lahkale R., and Sabbar E. (2025) Tungstate intercalated Mg-Al layered double hydroxide and its derived mixed metal oxide: preparation, characterization, and investigation of optical, electrical, and dielectric properties. *Clay Miner.*, 73(25) e9-e19.
21. Ameer S., Barhoumi A., Abdallaoui H. E. A. E., Syed A., Belghiti M. E., Elgorban A. M., Wong L. S., Wang S., El Idrissi M., Zeroual A., and Mazoir N. (2024) Molecular docking, exploring diverse selectivities and mechanistic insights in the cycloaddition reaction between 3-benzoylpyrrolo-[1, 2-a] quinoxaline-1, 2, 4 (5H)-triones and butyl vinyl ether. *Chem. Heterocycl. Compd.*, 60(11) 584-591.
22. Ameer S., Kačka-Zych A., Moussa Z., Alsantali R. I., Zeroual A., Alluhaibi M. S., Alsimaree A. A., and Ahmed S. A. (2025) Study of 1, 3-Dipolar Cycloaddition Between 4-Acyl-1H-pyrrole-2, 3-diones Fused at the [e]-Side with a Heterocyclic Moiety and Diphenylnitrone: A Comprehensive MEDT, Docking Approach and MD Simulation. *Mol.*, 30 (18) 3718-3739.
23. Ameer S., Barhoumi A., Ríos-Gutiérrez M., Aitouna A. O., Abdallaoui H. E. A. E., Mazoir N., Belghiti M. E., Syed A., Zeroual A., and Domingo L. R. (2023) A MEDT study of the mechanism and selectivity of the hetero-Diels–Alder reaction between 3-benzoylpyrrolo [1, 2-c][1, 4]-benzoxazine-1, 2, 4-trione and vinyl acetate. *Chem. Heterocycl. Compd.*, 59(3) 165-170.
24. Taha D. K., Hilal I. H., and Jabbar R. H. (2021) Theoretical properties of Ni2Ti alloys studied: By Gaussian 09 program. *J. Phys.: Conf. Ser.*, 1818(1) 012054-012059
25. Kartal Z., and Kartal K. (2023) A useful utility program for all Gaussian version users: ZEKA. *Journal of Scientific Reports-A*, 25(061) 25-33.
26. Sahrane M., Boutadghart T., Mennas I., Arif A., El idrissi M., and Ghailane R. (2026) Investigation of pyridazine derivatives as potential candidates against HIV-1 using ADMET analysis and molecular docking. *Curr. Chem. Lett.*, Accepted Manuscript (DOI: 10.5267/j.ccl.2026.1.001)
27. Parr R. G., Szentpály L. V., and Liu S. (1999) Electrophilicity index. *J. Am. Chem. Soc.*, 121(9) 1922-1924.
28. Parr R. G., and Pearson R. G. (1983) Absolute hardness: companion parameter to absolute electronegativity. *J. Am. Chem. Soc.*, 105(26) 7512-7516.
29. Domingo L. R., Chamorro E., and Pérez P. (2008) Understanding the reactivity of captodative ethylenes in polar cycloaddition reactions. A theoretical study. *J. Org. Chem.*, 73(12) 4615-4624.
30. Sadowski M., and Kula K. (2024) Unexpected course of reaction between (1E, 3E)-1, 4-Dinitro-1, 3-butadiene and n-methyl azomethine ylide—a comprehensive experimental and quantum-chemical study. *Molecules*, 29(21) 5066-5090.
31. Mtiraou H., Ghabi A., Al-Ghulikah H., Habib M. A., and Hajji M. (2024) Structural and chemical reactivity insights of a benzimidazolidinone-based N-heterocycle: A multiapproach quantum-chemical study. *Chem. Heterocycl. Compd.*, 60 (11) 611-616.
32. Curtiss L. A., McGrath M. P., Blaudeau J. P., Davis N. E., Binning Jr R. C., and Radom L. (1995) Extension of Gaussian-2 theory to molecules containing third-row atoms Ga–Kr. *J. Chem. Phys.*, 103(14) 6104-6113.
33. Du Q., and Arteca G. A. (1996) Modeling lipophilicity from the distribution of electrostatic potential on a molecular surface. *J. Comput. Mol. Des.*, 10(2) 133-144.
34. Chamorro E., Pérez P., and Domingo L. R. (2013) On the nature of Parr functions to predict the most reactive sites along organic polar reactions. *Chem. Phys. Lett.*, 582(13) 141-143.
35. Noureddine O., Issaoui N., Medimagh M., Al-Dossary O., and Marouani H. (2021) Quantum chemical studies on molecular structure, AIM, ELF, RDG and antiviral activities of hybrid hydroxychloroquine in the treatment of COVID-19: Molecular docking and DFT calculations. *J. King Saud Univ. Sci.*, 33(2) 101334-101346.
36. Daina A., Michielin O., and Zoete V. (2017) SwissADME: a free web tool to evaluate pharmacokinetics, drug-likeness and medicinal chemistry friendliness of small molecules. *Sci. Rep.*, 7(1) 42717-42730.
37. Pires D. E., Blundell T. L., and Ascher D. B. (2015) pkCSM: predicting small-molecule pharmacokinetic and toxicity properties using graph-based signatures. *J. Med. Chem.*, 58(9) 4066-4072.
38. Flachsenberg F., Ehrh C., Gutermuth T., and Rarey M. (2023) Redocking the PDB. *J. Chem. Inf. Model.*, 64(1) 219-237.



© 2026 by the authors; licensee Growing Science, Canada. This is an open access article distributed under the terms and conditions of the Creative Commons Attribution (CC-BY) license (<http://creativecommons.org/licenses/by/4.0/>).